



RESEARCH ARTICLE

10.1029/2021JA029611

Key Points:

- We compare proton bulk velocities and temperatures in the Venus plasma environment during solar minimum and maximum
- We measure lower perpendicular and parallel proton temperatures in Venus' magnetosheath during solar maximum than during solar minimum
- The spatial distribution of the temperature anisotropy is consistent with the observed growth and decay of mirror modes in the magnetosheath

Correspondence to:

S. Rojas Mata,
sebastian.rojasmata@irf.se

Citation:

Rojas Mata, S., Stenberg Wieser, G., Futaana, Y., Bader, A., Persson, M., Fedorov, A., & Zhang, T. (2022). Proton temperature anisotropies in the Venus plasma environment during Solar minimum and maximum. *Journal of Geophysical Research: Space Physics*, 127, e2021JA029611. <https://doi.org/10.1029/2021JA029611>

Received 28 MAY 2021
 Accepted 18 DEC 2021

© 2021. The Authors.

This is an open access article under the terms of the [Creative Commons Attribution-NonCommercial-NoDerivs License](https://creativecommons.org/licenses/by/4.0/), which permits use and distribution in any medium, provided the original work is properly cited, the use is non-commercial and no modifications or adaptations are made.

Proton Temperature Anisotropies in the Venus Plasma Environment During Solar Minimum and Maximum

Sebastián Rojas Mata¹ , Gabriella Stenberg Wieser¹ , Yoshifumi Futaana¹ , Alexander Bader² , Moa Persson³ , Andrey Fedorov³, and Tielong Zhang⁴ 

¹Swedish Institute of Space Physics, Kiruna, Sweden, ²Department of Physics, Lancaster University, Antwerp, Belgium, ³Institut de Recherche en Astrophysique et Planétologie, CNRS-UPS-CNES, Toulouse, France, ⁴Space Research Institute, Austrian Academy of Science, Graz, Austria

Abstract The proton population in Venus' plasma environment is characterized during periods of solar minimum and maximum using data from a particle mass-energy spectrometer. Such characterizations at different levels of solar activity provides physical insight into solar-cycle-dependent plasma phenomena around the planet, for example mirror modes in the magnetosheath. Statistical distributions of proton bulk speeds and temperatures are generated using a previously developed method which applies Maxwellian fits to measurements of the protons' velocity distribution function. Spatial maps and probability-density histograms comparing the proton parameters between the two time periods are presented. The temperatures perpendicular (T_{\perp}) and parallel (T_{\parallel}) to the background magnetic field are found to be 20%–35% lower during solar maximum. Though the overall distributions of the temperature ratio T_{\perp}/T_{\parallel} do not change, the regions with higher anisotropy ($T_{\perp}/T_{\parallel} > 1$) are found farther downstream from the bow shock during solar maximum than minimum. This is consistent with the previously observed growth of mirror modes during solar maximum and their decay during minimum.

1. Introduction

Though comparable to Earth in its size, internal structure, and distance from the Sun, Venus lacks an intrinsic magnetic field, thus allowing the solar wind to closely interact with its atmosphere and generate interesting plasma phenomena (Futaana et al., 2017). For example, as the solar wind is diverted around Venus, the interplanetary magnetic field (IMF) drapes around the planet and generates currents in the ionosphere, resulting in an induced magnetosphere. The extent of this magnetosphere is much smaller (~ 0.05 Venus radii at the subsolar point) than that of Earth's magnetosphere (~ 10 Earth radii) (Russell et al., 2016), but still provides a dayside magnetic barrier that diverts the solar wind's flow, causes the IMF field lines to pile up, and forms an upstream bow shock (Luhmann, 1986; Zhang et al., 1991). Studying such phenomena at Venus provides insight into how other unmagnetized atmospheric bodies interact with magnetized plasma flows, either in our Solar System (e.g., Mars or Titan (Bertucci et al., 2011; Brain et al., 2016)) or around other stars (Dong, Jin, et al., 2017; Dong, Lingam, et al., 2017). Additionally, Venus provides a valuable case study for investigating the role an intrinsic magnetic field may or may not play in a planet's eon-long atmospheric evolution (Gunell et al., 2018; Lundin et al., 2007).

Over shorter timescales, the solar-activity correlations exhibited by heliospheric parameters such as the magnitude of the IMF, the extreme ultraviolet (EUV) flux, or the f10.7 index (Gazis, 1996; Papitashvili et al., 2000; Russell et al., 1988) cause solar-cycle variations in Venus' plasma environment and plasma phenomena. For example, the location and shape of the bow shock varies with EUV flux (Russell et al., 1988; Whittaker et al., 2010; Zhang et al., 2008) while the density of the nightside ionosphere is affected by EUV flux, solar wind dynamic pressure, and the f10.7 index (Brace et al., 1990; Collinson et al., 2021; Theis & Brace, 1993). EUV flux also influences the outflow and circulation patterns of atmospheric hydrogen and oxygen ions in Venus' magnetotail (Kollmann et al., 2016; Persson et al., 2018). The level of solar activity even affects collective plasma phenomena such as mirror modes (Volwerk, Schmid, et al., 2016), upstream proton cyclotron waves (Delva et al., 2015), and low-frequency magnetic-field fluctuations in the magnetosheath and magnetotail (Xiao et al., 2017).

Among these phenomena, mirror modes are particularly interesting since they are ubiquitous in space plasmas, having been detected in planetary magnetosheaths (Bavassano Cattaneo et al., 1998; Espley et al., 2004; Joy et al., 2006; Russell & Song, 1989; Tsurutani et al., 1982), cometary environments (Russell et al., 1987; Tsurutani et al., 1999; Volwerk, Richter, et al., 2016), and interplanetary space (Tsurutani et al., 1992, 2011).

They may affect dayside magnetopause reconnection (Laitinen et al., 2010), however their influence on global magnetospheric physics is still unclear (Hoilijoki et al., 2016). Mirror modes around Venus were first detected (Volwerk et al., 2008) using magnetometer data (Zhang et al., 2006) collected during the Venus Express (VEX) mission (Svedhem et al., 2007). This mode is a low-frequency ion instability that may appear in high- β plasmas (where β is the ratio of thermal to magnetic energy-densities) with higher temperatures perpendicular to the background magnetic field than parallel to it, that is $T_{\perp}/T_{\parallel} > 1$ (Hasegawa, 1969; Tajiri, 1967). Derived in the long-parallel-wavelength limit, this nonoscillatory mode exhibits an anticorrelation between perturbations to the background magnetic field and perturbations to the perpendicular thermal energy density (Southwood & Kivelson, 1993). Ideally, identifying the mode involves magnetic-field and plasma data. However, often plasma data is not available or does not have sufficient time resolution to discern the mirror structures, so many studies of these wave modes only use magnetic-field measurements (Joy et al., 2006; Tsurutani et al., 2011).

One such study of mirror modes at Venus used VEX magnetometer data to detect mirror-mode events during solar minimum (24 May–31 December 2006) and solar maximum (1 November 2011–10 June 2012) (Volwerk, Schmid, et al., 2016). Notable among the findings was that mirror-mode structures presumably generated at the bow shock during solar minimum strictly decay as the solar wind convects them into the magnetosheath, whereas during solar maximum they first grow and then decay. The authors note that “[u]nfortunately, there are no papers discussing the plasma properties of Venus’s magnetosheath for solar minimum and maximum” to provide a physical explanation for these observed differences.

In this paper we address this gap by characterizing the proton population in Venus’ plasma environment using data collected during the entire VEX mission (2006–2014). We adopt a previously developed methodology which initially analyzed data collected during solar minimum (Bader et al., 2019); we extend the analysis to include measurements taken during solar maximum. We begin in Section 2 with an overview of the spectrometer and data set followed by a brief description of the methodology in Section 3. We present and compare spatial maps and probability-density histograms of the plasma parameters during solar minimum and maximum in Section 4. In Section 5 we use these results to provide new physical insight into observations of mirror modes in Venus’ magnetosheath and present concluding remarks in Section 6.

2. Instrument and Data Set

We use data collected by the Ion Mass Analyzer (IMA) instrument, a cylindrically-symmetric ion mass-energy spectrometer which was part of the Analyzer of Space Plasmas and Energetic Atoms (ASPERA-4) experiment on board VEX (Barabash et al., 2007). IMA measures particle counts in 192-s scans over 32 mass-per-charge channels (up to 80 amu/q with moderate mass-resolution $M/dM \gtrsim 1$), 96 logarithmic energy-per-charge steps (~ 0.01 –30 keV/q), and 16 azimuth \times 16 elevation angles spanning a 360×90 field of view. Each scan therefore provides particle counts in up to $32 \times 96 \times 16 \times 16 = 786,432$ distinct pixels in the instrument’s mass-azimuth-energy-elevation (M, E, Φ, Θ) parameter space. In this study we only use proton data so we work in a reduced (E, Φ, Θ) parameter space. We use total proton counts as further separation into solar-wind and planetary protons is not readily available. The mass-separation procedure (Fränz et al., 2006) helps remove the trace presence of alpha particles, which can artificially increase the temperatures calculated from less processed data (Halekas et al., 2017). We complement the IMA data with concurrent 1-s-resolution magnetic-field-vector measurements taken by the Venus Express Magnetometer (MAG) (Zhang et al., 2006).

3. Methodology

3.1. Fitting Algorithm

We first convert each scan’s counts $c(E, \Phi, \Theta)$ into particle differential flux

$$J(E, \Phi, \Theta) = \frac{c(E, \Phi, \Theta)}{G(E, \Phi, \Theta) \tau E}, \quad (1)$$

where G is the instrument’s geometric factor and $\tau = 120.9$ ms is IMA’s duty time for a single pixel. We then convert into phase-space density to calculate the velocity distribution function (VDF) (Fränz et al., 2006)

Table 1
Filtering of the 325,734 Scans

Scans with...	Number (% of Total)	Marginal decrease
more than 100 pixels available for drifting Maxwellian fit	296,729 (91%)	9%
IoA > 0.65 for drift Maxwellian fit	262,384 (81%)	12%
more than 100 pixels available for gyrotropic Maxwellian fit	258,052 (79%)	2%
IoA > 0.65 for gyrotropic Maxwellian fit	109,075 (33%)	58%

$$f(v_x, v_y, v_z) = \frac{m_p^2}{2E} J(E, \Phi, \Theta), \quad (2)$$

where m_p is the proton mass. Here we also transform from local IMA (E, Φ, Θ) coordinates to global Cartesian Venus Solar Orbit (VSO) velocity coordinates (v_x, v_y, v_z). Centered on Venus, the VSO frame has $+X_{VSO}$ pointing from Venus' center to the Sun, $+Z_{VSO}$ normal to Venus' orbital plane and pointing northward, and $+Y_{VSO}$ completing the right-handed system (i.e., antiparallel to the direction of Venus' orbital motion).

Instead of taking velocity-space moments of the proton VDFs to calculate plasma parameters (Fränz et al., 2006), we use the methodology developed by Bader et al. (2019) to derive physical parameters from Maxwellian fits to the VDF data. This has the advantage of compensating for an incomplete sampling of the VDF due to IMA's limited field of view. The fits also smooth the phase-space density measurements and the non-uniform (v_x, v_y, v_z) space. Maxwellian models have few fit parameters relative to the number of data points (which prevents overfitting) and correspond to a thermalized species with easily interpretable bulk parameters. Of course if the VDF is not adequately represented by a single Maxwellian (e.g., a non-thermalized species or a superposition of hot/cold or fast/slow populations) the methodology will produce poor results; the goodness-of-fit criteria detailed at the end of this section seek to filter out such poor fits.

Full details of the methodology are available in the reference; here we present a summary of the steps to process the proton VDF data of one 192-s IMA scan:

1. Fit a 3D drifting Maxwellian VDF with isotropic temperature to determine the proton bulk-velocity vector
2. Shift the data into the proton bulk-velocity frame (plasma frame)
3. Convert from Cartesian (v_x, v_y, v_z) to spherical (v, φ, θ) velocity coordinates
4. Rotate into a frame where the average local-magnetic-field vector $\bar{\mathbf{B}}_{IMF}$ lies along the $\theta = 0$ axis (i.e., θ is the pitch angle)
5. Convert from spherical (v, φ, θ) to local-magnetic-field (v_{\perp}, v_{\parallel}) velocity coordinates (we do not distinguish between different perpendicular directions)
6. Fit a gyrotropic Maxwellian VDF to determine the proton density and the thermal velocities in the directions perpendicular and parallel to $\bar{\mathbf{B}}_{IMF}$

We use the orthogonal distance regression algorithm (Boggs & Rogers, 1989) as implemented in SciPy's ODRPACK software package (SciPy, 2021) to fit the data. We only attempt to fit scans in which at least 100 of IMA's pixels recorded non-zero counts (after noise reduction), meaning that the corresponding VDF has at least 100 non-zero values. Additionally, after converting from Cartesian to spherical velocity coordinates, we remove pixels whose width ($\Delta E, \Delta \Phi, \Delta \Theta$) corresponds to a differential volume ($\Delta v, \Delta \varphi, \Delta \theta$) with $\Delta \theta > \pi/4$. This removes pixels with a pitch-angle uncertainty larger than 45.

3.2. Quality Metrics and Sources of Error

Bader et al. (2019) use the modified index of agreement (IoA) (Legates & McCabe, 1999) to quantify the goodness-of-fit of each scan's fits. We also adopt this metric and use their empirically determined value of 0.65 as the minimum value to consider a fit successful. We show in Table 1 how this metric along with the requirement for at least 100 pixels with non-zero counts progressively remove scans from the fitting process. The greatest loss occurs due to insufficiently good gyrotropic Maxwellian fits. Since we do not assess the stability of the IMF during the IMA scan, converting into a local-magnetic-field frame (defined by $\bar{\mathbf{B}}_{IMF}$ or otherwise) may be an

ill-posed task. A rapidly changing IMF (relative to IMA's 192-s cadence) may account for the lower success of the gyrotopic Maxwellian fit.

Bader et al. (2019) investigated several possible sources of error for the calculated proton parameters (see their Section 4.7). For example, the varying relative orientation between the spacecraft and $\overline{\mathbf{B}}_{IMF}$ may produce overestimated proton temperatures due to an inadequate extrapolation of partly sampled VDFs. We verified that their value of 0.65 for the modified IoA also suffices to suppress this effect in our fits. They also assessed the effect IMA's angular resolution ($22.5^\circ \times 4.5^\circ$ per pixel) has on the lowest resolvable temperature by applying the fitting algorithm to modeled Maxwellian VDFs. Since we use the same procedure their finding that temperatures down to 6 eV can be resolved for average solar wind flows (400 km/s) also applies to our work. Lastly, the spacecraft potential (which was not measured on VEX) could affect measured particle energies by shifting IMA's energy scale. They found that correcting the data for a spacecraft potential on the order of ± 5 V as estimated by models "did not produce significantly different results" (Bader et al., 2019), so the correction was not used in the study. We also do not correct for spacecraft potential since the associated $\lesssim 30$ km/s shift in particle velocities is within our error estimates (see Section 4.2).

Successful fits may nevertheless yield results that are not physically sensible (e.g., very high bulk velocities) or outside the instrument's reliable range of measurement (e.g., very low thermal velocities). Consequently, Bader et al. (2019) also suggest a series of physical and instrument-based criteria to further filter out poor fits. These include requiring that

1. The perpendicular and parallel temperatures are both below 700 eV
2. The bulk velocity is less than 1,000 km/s, and
3. The bulk velocity and both thermal velocities are above 20 km/s

The impact of these additional criteria on the results of our statistical study depends on the plasma region considered (e.g., the magnetotail vs. the upstream solar wind), so we postpone its discussion until Section 4.2 and first provide a global picture of the Venus plasma environment.

4. Results

For our comparative study scans taken during 2006–2009 belong to solar minimum (133,286 total, 62,527 with successful fits) and those taken during 2010–2014 inclusive to solar maximum (192,448 total, 46,548 with successful fits). The difference in percentage of successful fits between the two periods (47% vs. 24%) may imply more turbulent plasma conditions during solar maximum and therefore less Maxwellian-looking measurements. However we did not investigate the matter further. The following plots for solar minimum are not those from Bader et al. (2019), but rather the results of our new implementation of the fitting methodology. However, the two sets of results for that period show good agreement.

4.1. Spatial Maps for Solar Minimum and Maximum

We sort our results into spatial bins defined in a cylindrical VSO coordinate frame in which X_{VSO} is the axis of symmetry and the other two coordinates collapse into the radial coordinate $R_{VSO} = \sqrt{Y_{VSO}^2 + Z_{VSO}^2}$. We assume this symmetry about the X_{VSO} axis since, similarly to Bader et al. (2019), we did not observe significant asymmetries between the dawn/dusk and north/south sectors of the Cartesian VSO frame. Each bin measures $0.2 R_V \times 0.2 R_V$; together they span the domain $(X_{VSO}, R_{VSO}) \in [-3R_V, 2R_V] \times [0, 3R_V]$, where R_V is Venus' radius. We report the median value of the parameters (except for the maps in Figure 1 (a) and (b)) in order to avoid adverse effects of poor fits that nevertheless manage to meet the goodness-of-fit criteria listed above.

Figure 1 (a) and (b) show the number of successfully fitted scans in each bin along with the average location of Venus' bow shock (BS) (as calculated by Whittaker et al. (2010) during solar minimum and by Russell et al. (1988) during solar maximum) and ion composition boundary (ICB) as calculated by Martinecz et al. (2008). There is decent spatial coverage for both time periods which enables our statistical study. Figure 1 (c) and (d) display the proton bulk speed along with superimposed unit vectors corresponding to the median direction of the flow. No significant differences between the two periods are evident; the proton flow is primarily in the $-X_{VSO}$ direction except in the magnetotail behind the planet. The unperturbed solar wind has bulk speeds between 300 and

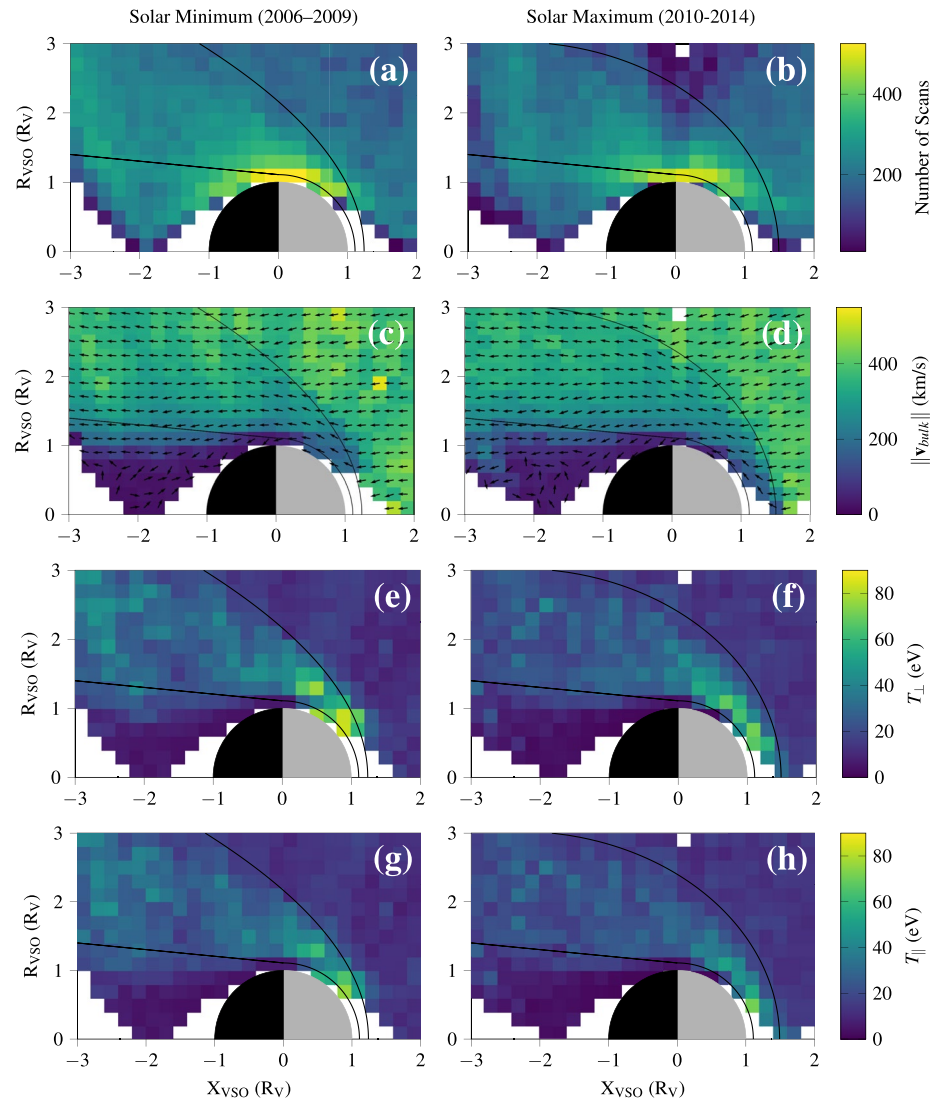


Figure 1. Spatial distributions of the number of successfully fitted scans and median proton bulk speeds, perpendicular temperatures T_{\perp} , and parallel temperatures T_{\parallel} during solar minimum and maximum. White areas are bins with less than 10 successfully fitted scans.

500 km/s, which drop by ~ 100 km/s after crossing the bow shock. In the wake region behind Venus proton bulk speeds are below 100 km/s.

Unlike the bulk velocity, the perpendicular and parallel temperatures in Figure 1 (e)–(h) show differences between the two time periods. Though similar in the unperturbed solar wind (~ 10 – 20 eV), both temperatures downstream of the bow shock are lower during solar maximum than minimum. To investigate these observations with greater detail, we analyze the distributions of the measurements in several physically relevant regions around the planet.

4.2. Comparative Histograms for Regions of Interest

Following Bader et al. (2019), we define the four regions of interest around Venus depicted in Figure 2. Since we do not determine the exact location of the BS and ICB, we omit bins that we deem too close to their average locations as it is unclear to which region the measurements belong. These appear as white areas in Figure 2, leaving the solar wind, flank magnetosheath, and magnetotail as our regions of interest. We also define a near-sub-solar magnetosheath region comprised of manually selected bins in the dayside magnetosheath where we expect the highest solar-wind pressure. We sort our data into these regions to create histograms of the measured parameters

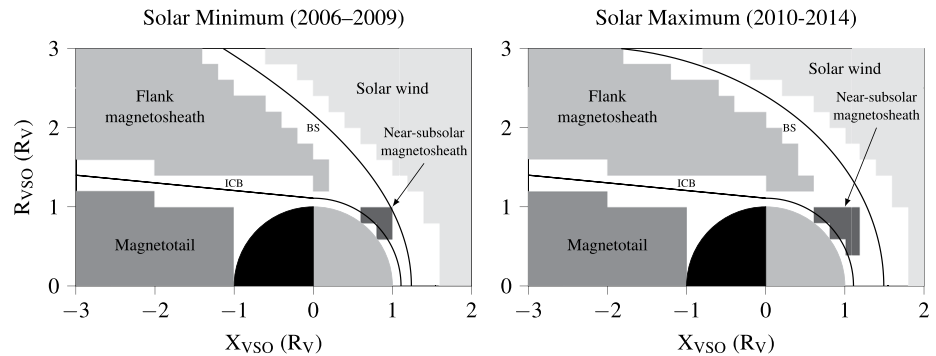


Figure 2. Plasma regions around Venus during solar minimum and maximum. The white areas indicate bins removed from our statistical analysis since their classification is indeterminate. The black lines depict the average locations of the bow shock (BS) and ion composition boundary (ICB) for each period.

and compare their distributions. Since different amounts of scans meet our goodness-of-fit criteria in each time period, we normalize them to produce probability density functions (PDFs) of the parameters. This accounts for differences in scale and provides clearer comparisons between the distributions.

We display in Figure 3 the distributions for the proton bulk speeds in the four regions. The median values are similar in each region during both time periods even though there are slight differences in the shape of the distributions. We also show a (rough) lower limit for the bulk speed reliably measured by IMA, here placed at 20 km/s as suggested by Bader et al. (2019). The probability of measuring bulk speeds below this limit in the solar wind and the flank magnetosheath is negligible compared to that of measuring bulk speeds in the 200–600 km/s range.

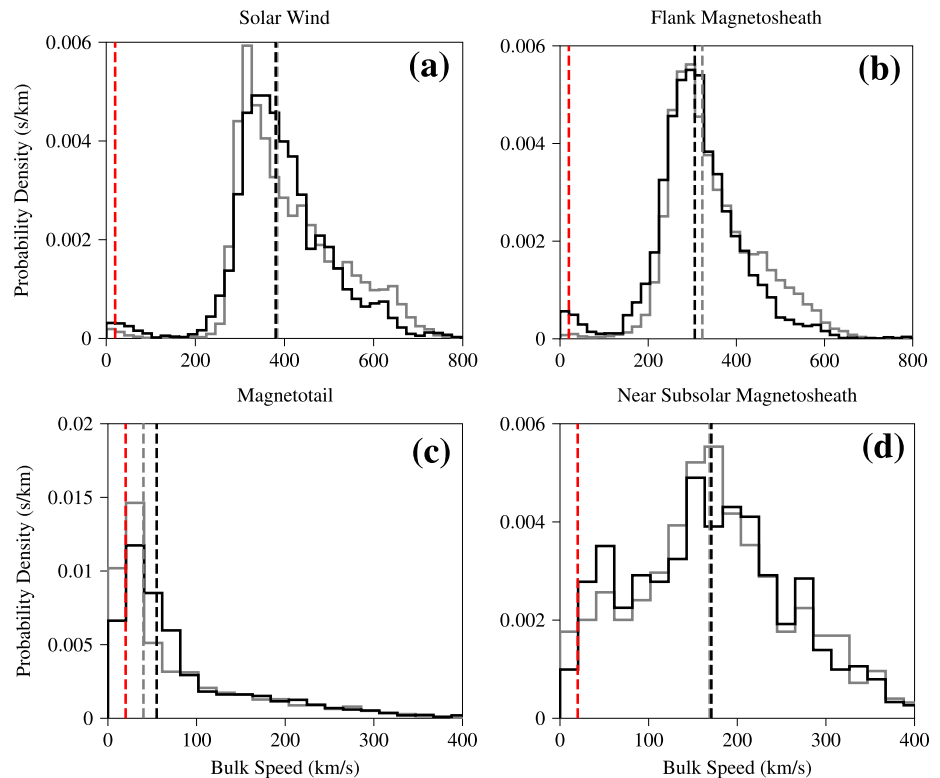


Figure 3. PDFs for the proton bulk speed in the four regions. Solid gray lines correspond to solar minimum values and black ones to solar maximum ones. The gray and black dashed lines indicate the medians during solar minimum and maximum, respectively. These medians are calculated using all the data. Data below the dashed red line at 20 km/s may not be suitable for physical interpretation. Bins are 20 km/s wide.

In the other two regions (especially the magnetotail), however, removing measurements below this limit affects the calculated medians and uncertainties (more details below).

In Figure 4 we show the distributions for the perpendicular and parallel proton temperatures in the four regions. In the solar wind, the two distributions of measurements are again quite similar. The distributions in the flank magnetosheath, however, indicate a clear increase in observations of lower temperature protons during solar maximum than minimum. This suggests that, even though the upstream solar wind has similar temperature profiles, as the protons cross the bow shock they are heated less during solar maximum than minimum. We observe a similar trend in the near-subsolar magnetosheath; the fewer observations in the region and their wider range of values produce less 'smooth' distributions. In the magnetotail lower temperatures are also more probable during solar maximum, though the change is less pronounced than in the two magnetosheath regions. We again mark a lower limit for the temperature reliably measured by IMA, here located at ~ 4 eV (i.e., 20 km/s thermal velocity for protons). Similar to the bulk speed, few measurements in the solar wind and flank magnetosheath lie below this limit.

We also calculate each scan's temperature ratio T_{\perp}/T_{\parallel} and compare their distributions in the different regions in Figure 5. No significant differences appear between the two time periods, finding an average anisotropy of $T_{\perp}/T_{\parallel} = 1.1\text{--}1.2$ in the magnetosheath regions. This indicates that the perpendicular and parallel temperatures decrease from one period to the next by the same ratio. Since we expect quasi-perpendicular and quasi-parallel shock geometries to lead to preferential perpendicular and parallel heating, respectively (Halekas et al. (2017) and references therein), the negligible change in T_{\perp}/T_{\parallel} may suggest that the relative occurrence of each configuration does not vary during the solar cycle. However, a characterization of our results as a function of shock geometry is needed to investigate this possibility. Despite this negligible change in the overall temperature anisotropy, in the next section we discuss how the spatial distribution of the temperature anisotropy relates to the observed growth and decay of mirror modes.

We summarize the median plasma parameters in the four regions in Table 2. To match our use of medians, we report uncertainties as median absolute deviations

$$\text{MAD} = \text{median}(|x_i - \text{median}(x_i)|) \quad (3)$$

of the measurements. The values in this table are calculated using all successful fits. If we remove fits using the additional criteria suggested by Bader et al. (2019) listed in Section 3, the parameter values and uncertainties in the solar wind and both magnetosheath regions do not change significantly. This is consistent with the low probability density of measurements below the instrument's limit for reliability in these regions. In the magnetotail, however, this additional filtering doubles the median values of the temperatures and reduces the corresponding MADs by 30%–50%. Similarly, the median magnitude of the bulk velocity and its MAD are increased by factors of 2–2.5. This applies to data from both time periods and indicates that the fitting methodology does not produce straightforwardly interpretable results in the magnetotail.

We note that Cycle 24's solar maximum was weaker than previous solar maxima (McComas et al., 2013), which means that the observed proton plasma parameters may not be representative of regular maxima. Varying our cutoff between minimum and maximum by a year or so does not affect the calculated parameters, indicating that the cutoff's value is not critical to observing the differences between the two periods. Characterizing the proton plasma as a function of upstream solar-wind parameters may provide results more easily compared to past solar maxima but such a task is beyond the scope of this study.

5. Discussion

Having characterized Venus' proton plasma environment during solar minimum and maximum, we now revisit Volwerk, Schmid, et al. (2016)'s observations of mirror modes in Venus' magnetosheath. The study identified mirror-mode events with 5–15 s periods during two individual Venusian years using only VEX magnetometer data; IMA's 192-s cadence is inadequate for capturing any corresponding density fluctuations. By statistically characterizing the modes' spatial distribution, strength, and growth/decay, the authors find that

1. 14% more events were detected during solar maximum than minimum (1,857 vs. 1,637)
2. The observational rate (events/time) was the same but with higher observational rates closer to the average bow shock during solar minimum

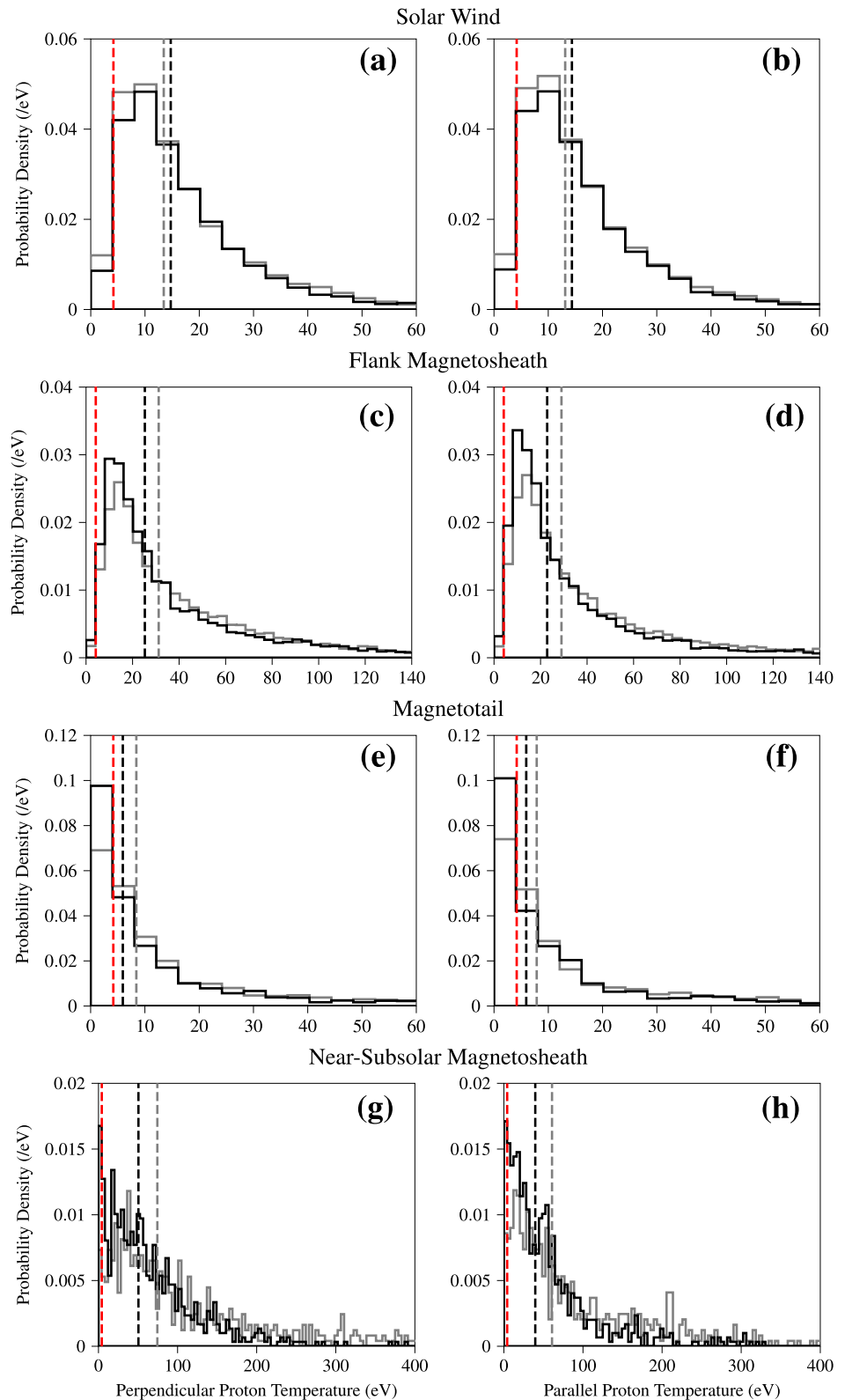


Figure 4. PDFs for the proton temperatures in the four regions. Solid gray lines correspond to solar minimum values and black ones to solar maximum ones. The gray and black dashed lines indicate the medians during solar minimum and maximum, respectively. These medians are calculated using all the data. Data below the dashed red line at ~ 4 eV (equivalent to a thermal velocity of 20 km/s for protons) may not be suitable for physical interpretation. Bins are 4 eV wide.

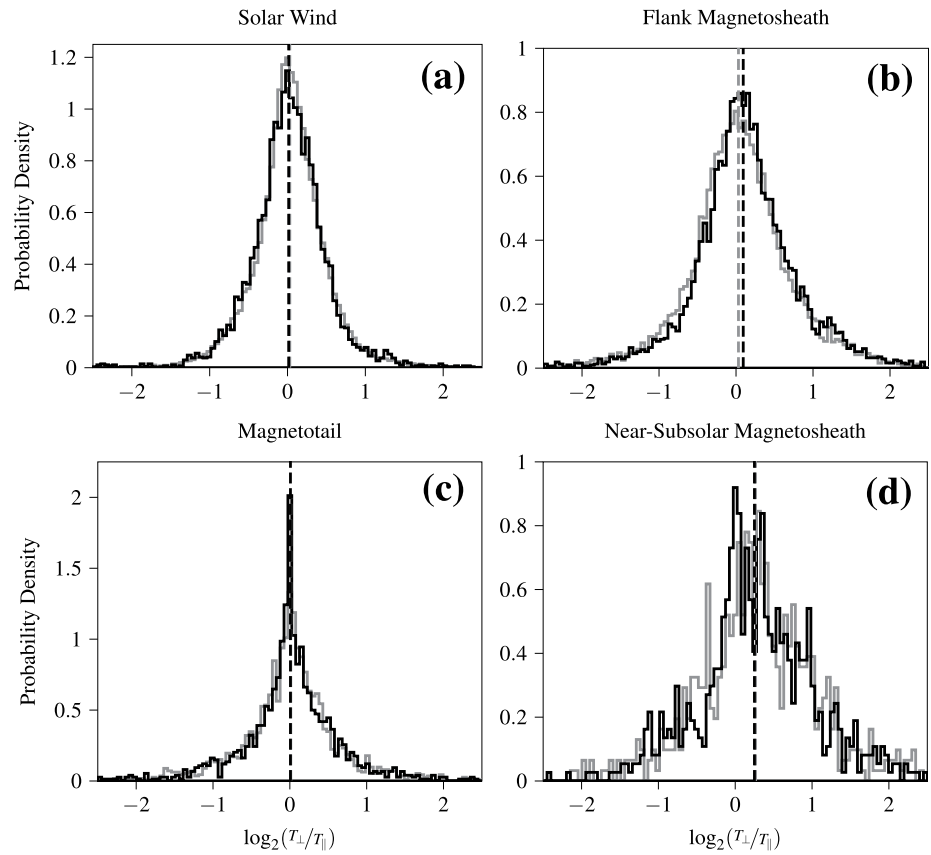


Figure 5. PDFs for proton temperature ratios in the four regions. Solid gray lines correspond to solar minimum values and black ones to solar maximum ones. The gray and black dashed lines indicate the medians during solar minimum and maximum, respectively. Bins are 0.05 wide in \log_2 space.

3. The strength of the waves was lower during solar maximum (though it is unclear if the difference is statistically significant), and
4. The mirror modes grew and then decayed as the solar wind convected them away from the BS during solar maximum, whereas during solar minimum they strictly decayed

The authors attribute the constant observational rate to a nearly constant upstream Alfvén Mach number (Delva et al., 2015), a parameter positively correlated with the occurrence of mirror modes in Earth's magnetosheath (Dimmock et al., 2015). They also argue that the detection of more events during solar maximum may be due to a larger magnetosheath region since the BS moves away from Venus during that period due to increased EUV

Table 2
Proton Parameters in the Regions Around Venus

	$\ \mathbf{v}_{bulk}\ $ (km/s)		T_{\perp} (eV)		T_{\parallel} (eV)		T_{\perp}/T_{\parallel}	
	Min	Max	Min	Max	Min	Max	Min	Max
SW	384 ± 71	380 ± 58	13 ± 6	15 ± 7	13 ± 6	14 ± 7	1.0 ± 0.2	1.0 ± 0.2
FMS	323 ± 58	306 ± 52	31 ± 18	25 ± 14	29 ± 17	23 ± 13	1.0 ± 0.2	1.1 ± 0.3
MT	40 ± 25	55 ± 30	8.4 ± 6	5.9 ± 4	7.9 ± 6	5.9 ± 4	1.0 ± 0.2	1.0 ± 0.2
NSMS	168 ± 59	171 ± 66	74 ± 47	51 ± 32	61 ± 44	40 ± 26	1.2 ± 0.4	1.2 ± 0.3

Note. T_{\perp}/T_{\parallel} is the median of the ratios, not the ratio of the medians. SW, Solar Wind; FMS, Flank Magnetosheath; MT, Magnetotail; NSMS, Near-Subsolar Magnetosheath.

ionization (Delva et al., 2015; Zhang et al., 2008). We use our results to characterize various parameters pertinent to the mirror mode's stability and provide new physical insight into the observations.

In a single-ion-species plasma, the instability criterion for the mirror mode is given by (Hasegawa, 1969)

$$1 + \beta_{\perp} \left(1 - \frac{T_{\perp}}{T_{\parallel}} \right) < 0, \quad (4)$$

where

$$\beta_{\perp} = \frac{nT_{\perp}}{B_0^2/2\mu_0} \quad (5)$$

is the perpendicular plasma beta with n the plasma density and B_0 the background magnetic field. Note that the mode is unstable for any β_{\perp} given sufficiently large T_{\perp}/T_{\parallel} , but T_{\perp}/T_{\parallel} must be greater than 1 for instability regardless of β_{\perp} (i.e., temperature anisotropy is a necessary but not sufficient condition for instability). Using these expressions, we present in Figure 6 the spatial distributions of the median values of the magnitude of the IMF, the perpendicular plasma beta, and the temperature ratio, along with the fraction of successfully fitted scans that meet the instability criterion.

We first note that the stronger compression of the magnetic field and lower perpendicular temperatures during solar maximum generate the much lower β_{\perp} plasma in the magnetosheath. Since our measurements of the distributions of T_{\perp}/T_{\parallel} in Figure 5 show no significant differences between solar minimum and maximum, the lower β_{\perp} seems to be the cause for the lower fraction of scans meeting the instability criterion during solar maximum. We might then expect a lower observational rate during this time period, which is contrary to observation (2) above. The claim in Volwerk, Richter, et al. (2016) about a larger magnetosheath during maximum may explain observation (1); exploring this idea further requires locating BS and ICB crossings instead of using average models. Such a task is beyond the scope of this statistical study given the amount of IMA scans being handled. Additionally, the different time intervals for the studies (1 Venus year vs. ~ 4 Earth years for each period) may in part account for the discrepancy. Restricting our data sets to match those of the study by Volwerk, Richter, et al. (2016) could give a fairer comparison but the resulting reduced data sets may not provide enough successful fits to conduct a statistically meaningful analysis.

Since observation (3)'s statistical significance is unclear we do not investigate connections between it and our characterization of Venus' plasma environment. Additionally, the presence of heavy ion species can affect the growth of electromagnetic ion instabilities like the mirror mode (Gary & Madland, 1988) so an analogous analysis of heavy ion VDFs may be necessary to investigate this observation further. We do note, however, that our measurements provide inputs for theoretical and numerical studies of the mirror mode's growth rate (Herčík et al., 2013; Hoilijoki et al., 2016; Kivelson & Southwood, 1996; Pokhotelov et al., 2008; Southwood & Kivelson, 1993).

Finally, the spatial distribution of T_{\perp}/T_{\parallel} provides physical insight into observation (4). During solar minimum, the regions with higher T_{\perp}/T_{\parallel} are closer to the average bow shock, which means the solar wind convects mirror modes formed close to the bow shock from a high-anisotropy region to a low-anisotropy one. Under these conditions we expect the modes to strictly decay as they travel into progressively stabler plasma, which agrees with Volwerk, Schmid, et al. (2016)'s observations. In contrast, during solar maximum the regions with higher T_{\perp}/T_{\parallel} are farther in the magnetosheath, so mirror modes formed close to the bow shock travel through regions of increasing anisotropy and instability before eventually reaching the region of decreasing anisotropy. In this case we expect the modes to initially grow before decaying closer to the terminator plane, again agreeing with Volwerk, Schmid, et al. (2016)'s observations.

6. Conclusions

In this paper we improved an existing methodology for calculating proton plasma parameters through Maxwellian fits of VDF measurements to analyze VEX IMA data taken during solar minimum (2006–2009) and maximum (2010–2014). We found lower perpendicular and parallel temperatures in the magnetosheath during solar maximum compared to minimum. Our work also indicated that the regions with higher temperature anisotropy in the flank magnetosheath were farther from the bow shock during solar maximum. This is consistent with previous

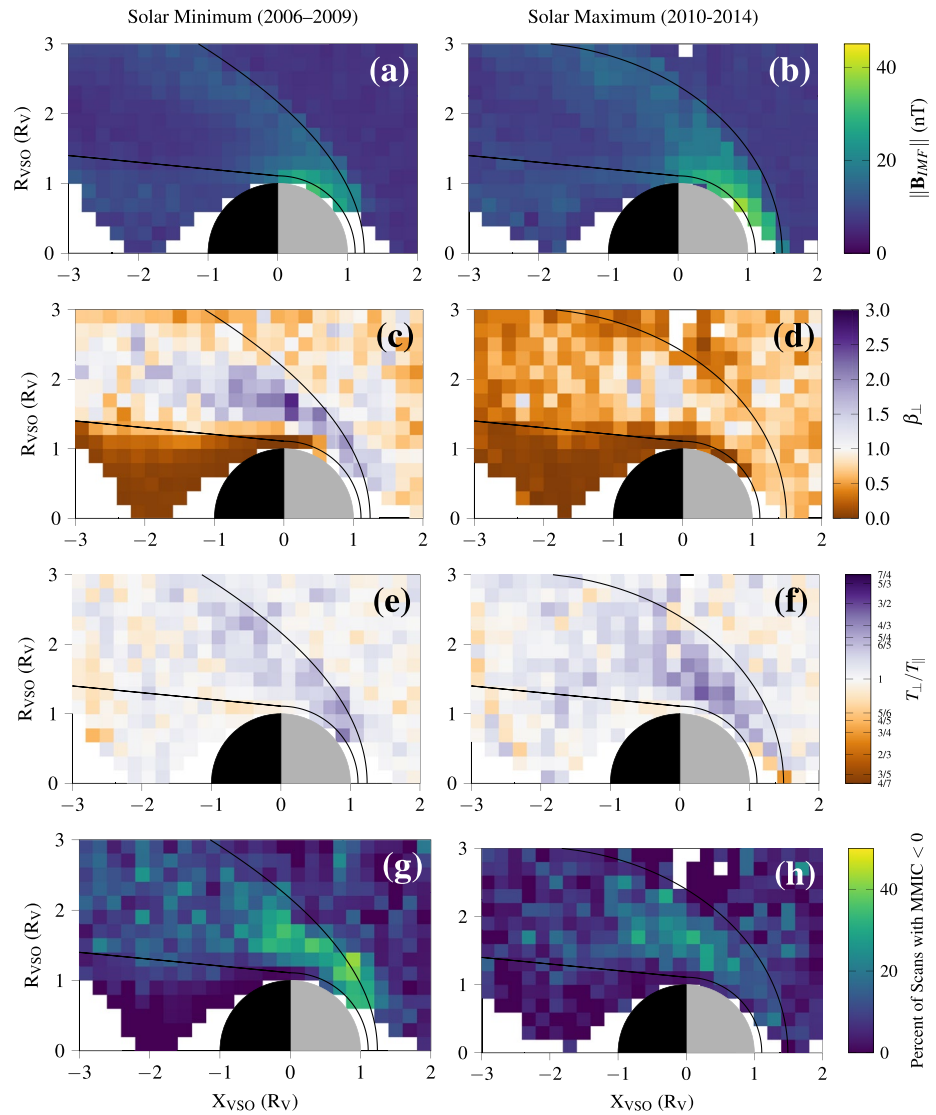


Figure 6. Spatial distribution of the magnitude of the IMF, the perpendicular plasma beta, the temperature ratio, and the fraction of successfully fitted VDFs which meet the instability criterion in Equation 4 during solar minimum and maximum. Values for the top three rows are medians.

observations of mirror modes growing and then decaying during solar maximum, whereas during solar minimum they purely decay.

A natural point to investigate further is *why* the proton temperatures are lower during solar maximum than minimum. Instead of analyzing the data in cylindrical VSO space, by using the location of the (average or orbit-by-orbit) bow shock as a reference point one could characterize the plasma parameters in more ‘physics-relevant’ frames (see, for example, Czaykowska et al. (2001) or Dimmock and Nykyri (2013)). Additionally, differentiating between quasi-parallel and quasi-perpendicular shock configurations can provide more detail regarding energy conversion mechanisms as these vary between the two shock geometries (Halekas et al., 2017; Russell et al., 2016; Scokopke et al., 1990). Investigating similar correlations with EUV flux levels and upstream solar-wind parameters (e.g., dynamic pressure or magnetosonic Mach number) could also be beneficial.

Data Availability Statement

All VEX data are publicly accessible at the ESA Planetary Science Archive at <https://www.cosmos.esa.int/web/psa/venus-express>.

Acknowledgments

SRM was funded by the Swedish National Space Agency under contracts 145/19 and 79/19.

References

- Bader, A., Stenberg Wieser, G., André, M., Wieser, M., Futaana, Y., Persson, M., et al. (2019). Proton temperature anisotropies in the plasma environment of Venus. *Journal of Geophysical Research: Space Physics*, *124*(5), 3312–3330. <https://doi.org/10.1029/2019JA026619>
- Barabash, S., Sauvaud, J. A., Gunell, H., Andersson, H., Grigoriev, A., Brinkfeldt, K., et al. (2007). The analyser of space plasmas and energetic Atoms (ASPERA-4) for the Venus express mission. *Planetary and Space Science*, *55*(12), 1772–1792. <https://doi.org/10.1016/j.pss.2007.01.014>
- Bavassano Cattaneo, M. B., Basile, C., Moreno, G., & Richardson, J. D. (1998). Evolution of mirror structures in the magnetosheath of Saturn from the bow shock to the magnetopause. *Journal of Geophysical Research*, *103*(A6), 11961–11972. <https://doi.org/10.1029/97ja03683>
- Bertucci, C., Duru, F., Edberg, N. J. T., Fränz, M., Martinecz, C., Szego, K., & Vaisberg, O. (2011). The induced magnetospheres of Mars, Venus, and Titan. *Space Science Reviews*, *162*(1–4), 113–171. <https://doi.org/10.1007/s11214-011-9845-1>
- Boggs, P., & Rogers, J. (1989). Orthogonal distance regression. In P. J. Brown, & W. A. Fuller (Eds.), *Statistical analysis of measurement error models and applications: Proceedings of the ams-ims-siam joint summer research conference held June 10-16, 1989* (pp. 183–194). Contemporary Mathematics. <https://doi.org/10.6028/nist.ir.89-4197>
- Brace, L. H., Theis, R. F., & Mihalov, J. D. (1990). Response of nightside Ionosphere and ionotail of Venus to Variations in solar EUV and solar wind dynamic pressure. *Journal of Geophysical Research*, *95*(A4), 4075–4084. <https://doi.org/10.1029/ja095ia04p04075>
- Brain, D. A., Bagenal, F., Ma, Y. J., Nilsson, H., & Stenberg Wieser, G. (2016). Atmospheric escape from unmagnetized bodies. *Journal of Geophysical Research: Planets*, *121*(12), 2364–2385. <https://doi.org/10.1002/2016JE005162>
- Collinson, G. A., Ramstad, R., Glocer, A., Wilson, L., & Brosius, A. (2021). Depleted plasma densities in the Ionosphere of Venus near solar minimum from Parker solar Probe observations of upper hybrid resonance emission. *Geophysical Research Letters*, *48*(9), 1–9. <https://doi.org/10.1029/2020GL092243>
- Czaykowska, A., Bauer, T. M., Treumann, R. A., & Baumjohann, W. (2001). Magnetic field fluctuations across the Earth's bow shock. *Annales Geophysicae*, *19*(3), 275–287. <https://doi.org/10.5194/angeo-19-275-2001>
- Delva, M., Bertucci, C., Volwerk, M., Lundin, R., Mazelle, C., & Rommanelli, N. (2015). Upstream proton cyclotron waves at venus near solar maximum. *Journal of Geophysical Research: Space Physics*, *120*(1), 344–354. <https://doi.org/10.1002/2014ja020318>
- Dimmock, A. P., & Nykyri, K. (2013). The statistical mapping of magnetosheath plasma properties based on THEMIS measurements in the magnetosheath interplanetary medium reference frame. *Journal of Geophysical Research: Space Physics*, *118*(8), 4963–4976. <https://doi.org/10.1002/jgra.50465>
- Dimmock, A. P., Osmane, A., Pulkkinen, T. I., & Nykyri, K. (2015). A statistical study of the dawn-dusk asymmetry of ion temperature anisotropy and mirror mode occurrence in the terrestrial dayside magnetosheath using THEMIS data. *Journal of Geophysical Research: Space Physics*, *120*(7), 5489–5503. <https://doi.org/10.1002/2015JA021192>
- Dong, C., Jin, M., Lingam, M., Airapetian, V. S., Ma, Y., & van der Holst, B. (2017). Atmospheric escape from the TRAPPIST-1 planets and implications for habitability. *Proceedings of the National Academy of Sciences of the United States of America*, *115*(2), 260–265. <https://doi.org/10.1073/pnas.1708010115>
- Dong, C., Lingam, M., Ma, Y., & Cohen, O. (2017). Is proxima Centauri b habitable? A study of atmospheric loss. *The Astrophysical Journal Letters*, *837*(L26), 1–6. <https://doi.org/10.3847/2041-8213/aa6438>
- Espley, J. R., Cloutier, P. A., Brain, D. A., Crider, D. H., & Acuña, M. H. (2004). Observations of low-frequency magnetic oscillations in the Martian magnetosheath, magnetic pileup region, and tail. *Journal of Geophysical Research*, *109*, A07213. <https://doi.org/10.1029/2003JA010193>
- Fränz, M., Dubinin, E., Roussos, E., Woch, J., Winningham, J. D., Frahm, R. A., et al. (2006). Plasma moments in the environment of Mars: Mars express ASPERA-3 observations. *Space Science Reviews*, *126*(1–4), 165–207. <https://doi.org/10.1007/s11214-006-9115-9>
- Futaana, Y., Stenberg Wieser, G., Barabash, S., & Luhmann, J. G. (2017). Solar wind interaction and impact on the Venus atmosphere. *Space Science Reviews*, *212*(3–4), 1453–1509. <https://doi.org/10.1007/s11214-017-0362-8>
- Gary, S. P., & Madland, C. D. (1988). Electromagnetic ion instabilities in a cometary environment. *Journal of Geophysical Research*, *93*(A1), 235. <https://doi.org/10.1029/ja093ia01p00235>
- Gaziz, P. R. (1996). Solar cycle variation in the heliosphere. *Reviews of Geophysics*, *34*(3), 379–402. <https://doi.org/10.1029/96RG00892>
- Gunell, H., Maggiolo, R., Nilsson, H., Stenberg Wieser, G., Slapak, R., Lindkvist, J., et al. (2018). Why an intrinsic magnetic field does not protect a planet against atmospheric escape? *Astronomy and Astrophysics*, *614*(L3), 1–8. <https://doi.org/10.1051/0004-6361/201832934>
- Halekas, J. S., Ruhunusiri, S., Harada, Y., Collinson, G., Mitchell, D. L., Mazelle, C., et al. (2017). Structure, dynamics, and seasonal variability of the Mars-solar wind interaction: MAVEN solar wind ion analyzer in-flight performance and science results. *Journal of Geophysical Research: Space Physics*, *122*(1), 547–578. <https://doi.org/10.1002/2016JA023167>
- Hasegawa, A. (1969). Drift mirror instability in the magnetosphere. *Physics of Fluids*, *12*(12), 2642–2650. <https://doi.org/10.1063/1.1692407>
- Herčík, D., Trávníček, P. M., Johnson, J. R., Kim, E. H., & Hellinger, P. (2013). Mirror mode structures in the asymmetric Helmean magnetosheath: Hybrid simulations. *Journal of Geophysical Research: Space Physics*, *118*(1), 405–417. <https://doi.org/10.1029/2012JA018083>
- Hoilijoki, S., Palmroth, M., Walsh, B. M., Pfau-Kempf, Y., von Alfthan, S., Ganse, U., et al. (2016). Mirror modes in the Earth's magnetosheath: Results from a global hybrid-Vlasov simulation. *Journal of Geophysical Research - A: Space Physics*, *121*(5), 4191–4204. <https://doi.org/10.1002/2015JA022026>
- Joy, S. P., Kivelson, M. G., Walker, R. J., Khurana, K. K., Russell, C. T., & Paterson, W. R. (2006). Mirror mode structures in the Jovian magnetosheath. *Journal of Geophysical Research*, *111*(12), 1–14, A12212. <https://doi.org/10.1029/2006JA011985>
- Kivelson, M. G., & Southwood, D. J. (1996). Mirror instability II: The mechanism of nonlinear saturation. *Journal of Geophysical Research*, *101*(A8), 17365–17371. <https://doi.org/10.1029/96ja01407>
- Kollmann, P., Brandt, P. C., Collinson, G., Rong, Z. J., Futaana, Y., & Zhang, T. L. (2016). Properties of planetward ion flows in Venus' magnetotail. *Icarus*, *274*, 73–82. <https://doi.org/10.1016/j.icarus.2016.02.053>
- Laitinen, T. V., Khotyaintsev, Y. V., André, M., Vaivads, A., & Réme, H. (2010). Local influence of magnetosheath plasma beta fluctuations on magnetopause reconnection. *Annales Geophysicae*, *28*(5), 1053–1063. <https://doi.org/10.5194/angeo-28-1053-2010>

- Legates, D. R. & McCabe, G. J. (1999). Evaluating the use of 'goodness-of-fit' measures in hydrologic and hydroclimatic model validation. *Water Resources Research*, 35(1), 233–241. <https://doi.org/10.1029/1998WR900018>
- Luhmann, J. G. (1986). The solar wind interaction with Venus. *Space Science Reviews*, 44, 241–306. <https://doi.org/10.1007/bf00200818>
- Lundin, R., Lammer, H., & Ribas, I. (2007). Planetary magnetic fields and solar forcing: Implications for atmospheric evolution. *Space Science Reviews*, 129, 245–278. <https://doi.org/10.1007/s11214-007-9176-4>
- Martinez, C., Fränz, M., Woch, J., Krupp, N., Roussos, E., Dubinin, E., et al. (2008). Location of the bow shock and ion composition boundaries at Venus—Initial determinations from Venus Express ASPERA-4. *Planetary and Space Science*, 56(6), 780–784. Retrieved from <https://www.sciencedirect.com/science/article/pii/S0032063307003765>. <https://doi.org/10.1016/j.pss.2007.07.007>
- McComas, D. J., Angold, N., Elliott, H. A., Livadiotis, G., Schwadron, N. A., Skoug, R. M., & Smith, C. W. (2013). Weakest solar wind of the space age and the current "mini" solar maximum. *The Astrophysical Journal*, 779(1), 2. <https://doi.org/10.1088/0004-637X/779/1/2>
- Papitashvili, V. O., Papitashvili, N. E., & King, J. H. (2000). Solar cycle effects in planetary geomagnetic activity: Analysis of 36-year long OMNI dataset. *Geophysical Research Letters*, 27(17), 2797–2800. <https://doi.org/10.1029/2000GL000064>
- Persson, M., Futaana, Y., Fedorov, A., Nilsson, H., Hamrin, M., & Barabash, S. (2018). H⁺/O⁺ escape rate ratio in the Venus magnetotail and its dependence on the solar cycle. *Geophysical Research Letters*, 45(20), 10805–10811. <https://doi.org/10.1029/2018GL079454>
- Pokhotelov, O. A., Sagdeev, R. Z., Balikhin, M. A., Onishchenko, O. G., & Fedun, V. N. (2008). Nonlinear mirror waves in non-Maxwellian space plasmas. *Journal of Geophysical Research*, 113, 1. <https://doi.org/10.1029/2007JA012642>
- Russell, C. T., Chou, E., Luhmann, J. G., Gazis, P., Brace, L. H., & Hoegy, W. R. (1988). Solar and interplanetary control of the location of the Venus bow shock. *Journal of Geophysical Research*, 93(A6), 5461. <https://doi.org/10.1029/ja093ia06p05461>
- Russell, C. T., Luhmann, J. G., & Strangeway, R. J. (2016). *Space physics: An introduction*. Cambridge University Press.
- Russell, C. T., Riedler, W., Schwingenschuh, K., & Yeroshenko, Y. (1987). Mirror instability in the magnetosheath of comet Halley. *Geophysical Research Letters*, 14(6), 644–647. <https://doi.org/10.1029/g1014i006p00644>
- Russell, C. T., Song, P., & Lepping, R. P. (1989). The uranian magnetopause: Lessons from Earth. *Geophysical Research Letters*, 16(12), 1485–1488. <https://doi.org/10.1029/g1016i012p01485>
- SciPy. (2021). *Orthogonal distance regression (scipy.odr)*. Retrieved from <https://docs.scipy.org/doc/scipy/reference/odr.html>
- Sckopke, N., Paschmann, G., Brinca, A. L., Carlson, C. W., & Lüth, H. (1990). Ion thermalization in quasi-perpendicular shocks involving reflected ions. *Journal of Geophysical Research*, 95(A5), 6337. <https://doi.org/10.1029/ja095ia05p06337>
- Southwood, D. J. & Kivelson, M. G. (1993). Mirror instability: 1. Physical mechanism of linear instability. *Journal of Geophysical Research*, 98(A6), 9181–9187. <https://doi.org/10.1029/92ja02837>
- Svedhem, H., Titov, D. V., McCoy, D., Lebreton, J. P., Barabash, S., Bertaux, J. L., et al. (2007). Venus express—The first European mission to Venus. *Planetary and Space Science*, 55(12), 1636–1652. <https://doi.org/10.1016/j.pss.2007.01.013>
- Tajiri, M. (1967). Propagation of Hydromagnetic waves in collisionless plasma. II. Kinetic approach. *Journal of the Physical Society of Japan*, 22(6), 1482–1494. <https://doi.org/10.1143/jpsj.22.1482>
- Theis, R. F., & Brace, L. H. (1993). Solar cycle variations of electron density and temperature in the Venesian nightside Ionosphere. *Geophysical Research Letters*, 20(23), 2719–2722. <https://doi.org/10.1029/93gl02485>
- Tsurutani, B. T., Lakhina, G. S., Smith, E. J., Buti, B., Moses, S. L., Coroniti, F. V., et al. (1999). Mirror mode structures and ELF plasma waves in the Giacobini-Zinner magnetosheath. *Nonlinear Processes in Geophysics*, 6, 229–234. <https://doi.org/10.5194/npg-6-229-1999>
- Tsurutani, B. T., Lakhina, G. S., Verkhoglyadova, O. P., Echer, E., Guarnieri, F. L., Narita, Y., & Constantinescu, D. O. (2011). Magnetosheath and heliosheath mirror mode structures, interplanetary magnetic decreases, and linear magnetic decreases: Differences and distinguishing features. *Journal of Geophysical Research*, 116(2), A02103. <https://doi.org/10.1029/2010JA015913>
- Tsurutani, B. T., Smith, E. J., Anderson, R. R., Ogilvie, K. W., Scudder, J. D., Baker, D. N., & Bame, S. J. (1982). Lion roars and nonoscillatory drift mirror waves in the magnetosheath. *Journal of Geophysical Research*, 87(A8), 6060. <https://doi.org/10.1029/ja087ia08p06060>
- Tsurutani, B. T., Southwood, D. J., Smith, E. J., & Balogh, A. (1992). Nonlinear magnetosonic waves and mirror mode structures in the March 1991 ulysses interplanetary event. *Geophysical Research Letters*, 19(12), 1267–1270. <https://doi.org/10.1029/92gl00782>
- Volwerk, M., Richter, I., Tsurutani, B. T., Götz, C., Altwegg, K., Broiles, T., et al. (2016). Mass-loading, pile-up, and mirror-mode waves at comet 67P/Churyumov-Gerasimenko. *Annales Geophysicae*, 34, 1–15. <https://doi.org/10.5194/angeo-34-1-2016>
- Volwerk, M., Schmid, D., Tsurutani, B. T., Delva, M., Plaschke, F., Narita, Y., et al. (2016). Mirror mode waves in Venus's magnetosheath: Solar minimum vs. solar maximum. *Annales Geophysicae*, 34(11), 1099–1108. <https://doi.org/10.5194/angeo-34-1099-2016>
- Volwerk, M., Zhang, T. L., Delva, M., Vörös, Z., Baumjohann, W., & Glassmeier, K.-H. (2008). First identification of mirror mode waves in Venus' magnetosheath? *Geophysical Research Letters*, 35(12), 1–n. <https://doi.org/10.1029/2008GL033621>
- Whittaker, I., Guymer, G., Grande, M., Pintér, B., Barabash, S., Federov, A., et al. (2010). Venesian bow shock as seen by the ASPERA-4 ion instrument on Venus Express. *Journal of Geophysical Research*, 115(9), A09224. <https://doi.org/10.1029/2009JA014826>
- Xiao, S. D., Zhang, T. L., & Wang, G. Q. (2017). Statistical study of low-frequency magnetic field fluctuations near Venus during the solar cycle. *Journal of Geophysical Research: Space Physics*, 122(8), 8409–8418. <https://doi.org/10.1002/2017JA023878>
- Zhang, T. L., Baumjohann, W., Delva, M., Auster, H.-U., Balogh, A., Russell, C. T., et al. (2006). Magnetic field investigation of the Venus plasma environment: Expected new results from Venus Express. *Planetary and Space Science*, 54(13), 1336–1343. Retrieved from <https://www.sciencedirect.com/science/article/pii/S0032063306001607>. <https://doi.org/10.1016/j.pss.2006.04.018>
- Zhang, T. L., Delva, M., Baumjohann, W., Volwerk, M., Russell, C. T., Barabash, S., et al. (2008). Initial Venus Express magnetic field observations of the Venus bow shock location at solar minimum. *Planetary and Space Science*, 56(6), 785–789. <https://doi.org/10.1016/j.pss.2007.09.012>
- Zhang, T. L., Luhmann, J. G., & Russell, C. T. (1991). The magnetic barrier at Venus. *Journal of Geophysical Research*, 96(A7), 11145–11153. <https://doi.org/10.1029/91ja00088>